Dual-Pol VPR Corrections for Improved Operational Radar QPE in MRMS

WOLFGANG HANFT,[a,b] JIAN ZHANG,[b] AND MICHEAL SIMPSON[a,b]

[a] Cooperative Institute for Severe and High-Impact Weather Research and Operations, University of Oklahoma, Norman, Oklahoma
[b] NOAA/OAR/National Severe Storms Laboratory, Norman, Oklahoma

ABSTRACT: The radar bright band is caused by melting ice crystals, and results in inflated reflectivity observations. If uncorrected, the bright band can result in large errors in radar-derived quantitative precipitation estimation (QPE). In the operational Multi-Radar Multi-Sensor (MRMS) system up to version 12.1, the effects of the bright band are corrected through the use of a reflectivity-only, tilt-based apparent vertical profile of reflectivity (tilt-VPR). This study utilizes dual-polarization (dual-pol) radar observations to improve the tilt-VPR methodology. To accomplish this, a brightband area delineation was developed within the MRMS framework and the brightband top and bottom heights were identified for individual tilts of radar data. This information was used to develop a radially dependent dual-pol VPR (dpVPR) model that can better correct reflectivity in situations of nonisotropic bright bands and low brightband events. This algorithm has been tested on 14 varying brightband events across the CONUS and compared with the tilt-VPR and the National Weather Service Weather Surveillance Radar-1988 Doppler Level-3 Digital Precipitation Rate (DPR) products. The radially dependent dpVPR correction provided a more accurate detection of brightband areas and a more effective reduction in QPE errors within and above the bright band than the tilt-VPR and DPR QPEs, especially for precipitation events with low melting layers or with strong variability of vertical motions. The brightband delineation and dpVPR methodology are also evaluated in the real-time MRMS testbed for their robustness and computational efficiency and has been transitioned into operations in 2022.

KEYWORDS: Precipitation; Hydrometeorology; Algorithms; Radars/Radar observations

1. Introduction

Radar-based quantitative precipitation estimation (QPE) has provided higher spatial and temporal resolution precipitation information than in situ gauge networks and is a critical data source for flash flood and river flood predictions and water resource management. Numerous methods have been developed for radar-based QPE, which utilize reflectivity (Z), differential reflectivity (Z_{DR}), specific differential phase (K_{DP}), and specific attenuation (A) (e.g., Marshall et al. 1947; Wilson and Brandes 1979; Joss et al. 1990; Fulton et al. 1998; Germann et al. 2006; Tabary 2007; Giangrande and Ryzhkov 2008; Wang et al. 2014; Zhang et al. 2016, 2020). Each of these methodologies has differing strengths and limitations; for example, specific-attenuation-based QPE is insensitive to radar calibration errors based on the technique proposed in Ryzhkov et al. (2014) but can only be applied in areas where the radar observes pure rain. While reflectivity-based QPE is not immune to the effects of calibration errors, it can be applied in liquid and frozen precipitation. Further, the reflectivity field can be inflated in areas of melting aggregated snow (the so-called "bright band," hereafter BB) and results in a radar rainfall overestimation if not corrected. Prior studies have shown the BB in stratiform rain follows a typical structure, where the peak in Z can reach 13 dBZ higher than that observed in the pure rain below it, and Z of rain is 1–2 dBZ higher than that of pure ice aloft (e.g., Kitchen et al. 1994; Fabry and Zawadzki 1995; Zhang et al. 2008). At far ranges from the radar, the radar beam can often overshoot the melting layer or even cloud tops. This results in low reflectivity values in the ice region above stratiform rain and subsequentially a radar QPE underestimation.

Numerous studies have developed methodologies for correcting reflectivity within and above the BB, typically done through a vertical profile of reflectivity (VPR). These studies include VPRs based on climatology (Koistinen 1991; Joss and Lee 1995), retrieved localized VPRs (Andrieu and Creutin 1995; Vignal et al. 1999), parameterized VPRs (Kitchen et al. 1994; Kitchen 1997), and VPRs from real-time volume scan data (Vignal et al. 2000; Zhang and Qi 2010; Koistinen and Pohjola 2014). All aforementioned VPRs were constructed using the operational weather radar data. Additional studies used external reference VPRs from profiler radars (e.g., Chen et al. 2020; Qi et al. 2014) to help further mitigate small-scale radar QPE errors in complex terrain. Giangrande and Ryzhkov (2008) developed an operational dual-polarization (dual-pol) synthetic QPE [i.e., the digital precipitation rate (DPR)] for the Weather Surveillance Radar-1988 Doppler (WSR-88D) network that included a non-VPR-based correction for range-dependent radar QPE errors. This empirical correction applies predefined multipliers to the rain rates derived from radar reflectivities within and above the BB based on hydrometer classifications (Park et al. 2009). The current study aims at an operational dual-pol-based VPR correction for national radar networks such as the WSR-88D using the radar data. It is intended to replace the single-pol VPR methodology developed by Zhang and Qi (2010) (referred to hereafter as "tilt-VPR") that uses reflectivity data from a single tilt scan to correct reflectivity. Their methodology allows for a tilt-VPR to be constructed quickly

---

Corresponding author: Jian Zhang, jian.zhang@noaa.gov

using the internal radar data in real time and accounts for temporal variations of BB strengths and intensities, an area where climatic VPRs can experience limitations. The tilt-VPR methodology is currently used to correct reflectivity in the Multi-Radar Multi-Sensor (MRMS) system (Zhang et al. 2016), which runs operationally in real time. Tilt-VPR reflectivity corrections within MRMS are done on a single radar basis. Corrected reflectivity from each radar in the domain are then merged together to create the seamless hybrid scan of reflectivity product (Zhang et al. 2016), and a radar-only QPE product is calculated from this field. Additionally, the corrected reflectivity is used in other MRMS QPE modules where an $R(Z)$ relationship is applied (specifically, in regions where ice is present).

The tilt-VPR methodology assumes that the BB structure is isotropic and is fully observed. These assumptions can fail in the presence of frontal boundaries with large variations of the melting layer height, and in cool seasons when the melting layer can be very low and the BB only partly observed. Additionally, the tilt-VPR methodology only utilizes reflectivity profiles. Isotropic BB in pure stratiform rain can typically be easily deduced from reflectivity alone, however, nonisotropic BB or those in complex wintery events may be hard to deduce using reflectivity alone. Due to the common dual-pol signatures within the melting layer, they can be leveraged to more accurately identify the BB area in most BB events. Additionally, the use of dual-pol variables and the delineation of the BB area can allow for more localized VPRs to be calculated, reducing errors in corrected reflectivity associated with nonisotropic BB.

To address QPE errors associated with nonisotropic BB, and very low melting layer events, this paper introduces a new methodology for a dual-pol azimuthally dependent vertical profile of reflectivity (dpVPR), which builds upon the work of Zhang and Qi (2010). Additionally, a new methodology is presented to delineate "apparent" areas (i.e., bright band) in the radar observations that are affected by a melting layer and then correct the bulk effect for more accurate QPE. The BB area delineation was not designed to retrieve the vertical structure of the atmospheric melting layer, though. The relation of a radar bright band and the atmospheric melting layer depends on many factors including the hydrometeors' falling and melting processes and the beam propagation and broadening patterns. A melting layer retrieval and validation requires additional observations (such as those from a profiling radar) and is beyond the scope of the current QPE study.

This methodology was developed and tested on case studies with varying BB structures, heights, and intensities, as well as in the real-time experimental MRMS system on the CONUS domain. The dpVPR QPEs were compared with the tilt-VPR and the DPR QPEs, both of which were running operationally for the WSR-88D network. The structure of this paper is as follows: in section 2, the methodology for the BB delineation algorithm, dpVPR construction, and reflectivity corrections using the dpVPR are presented. The results of the dpVPR corrections from case studies and real-time observations are discussed in section 3. Last, the summary, conclusions, and future work follow in section 4.
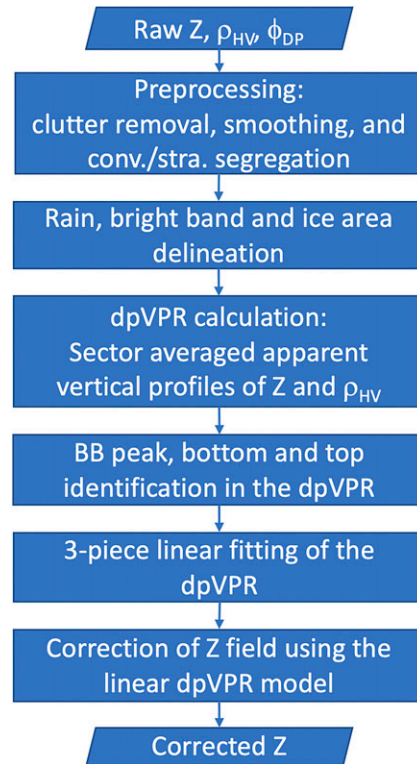

FIG. 1. An overview flowchart of the dpVPR methodology.

2. Methodology

Figure 1 shows an overview flowchart of the dpVPR methodology and detailed descriptions of each step are provided below.

a. Data preprocessing

This study utilizes Z, ρ_{hv} (correlation coefficient), and ϕ_{DP} (differential phase) data from the WSR-88D network, as well as from the Canadian S-band radar network. Radar data are initially quality controlled (QC) using the MRMS dual-pol QC algorithms (Tang et al. 2014, 2020). To reduce statistical noise common in dual-pol moments, radar variables are smoothed along the radial direction with an average filter of 3 km for reflectivity and 5 km for ρ_{HV} (Giangrande et al. 2008). The standard deviations, or texture parameters, of ϕ_{DP} and ρ_{hv} are also calculated using unsmoothed fields in a 9-gate radial segment. These texture parameters aid in the identification of ground clutter that may be present when precipitation is also occurring (Krause 2016). It is important to identify these gates because they often share similar dual-pol signatures as the BB and can result in erroneous identification of BB. Last, a convective–stratiform rain segregation function (Qi et al. 2013) is run to identify any areas of convection. Because of large differences in the vertical structure of convection compared to stratiform rain, convection should be identified before a BB is identified and a reflectivity correction is applied (Smyth and Illingworth 1998; Steiner et al. 1995; Zhang et al. 2008; Zhang and Qi 2010). Figures 2a–c show an example of the smoothed
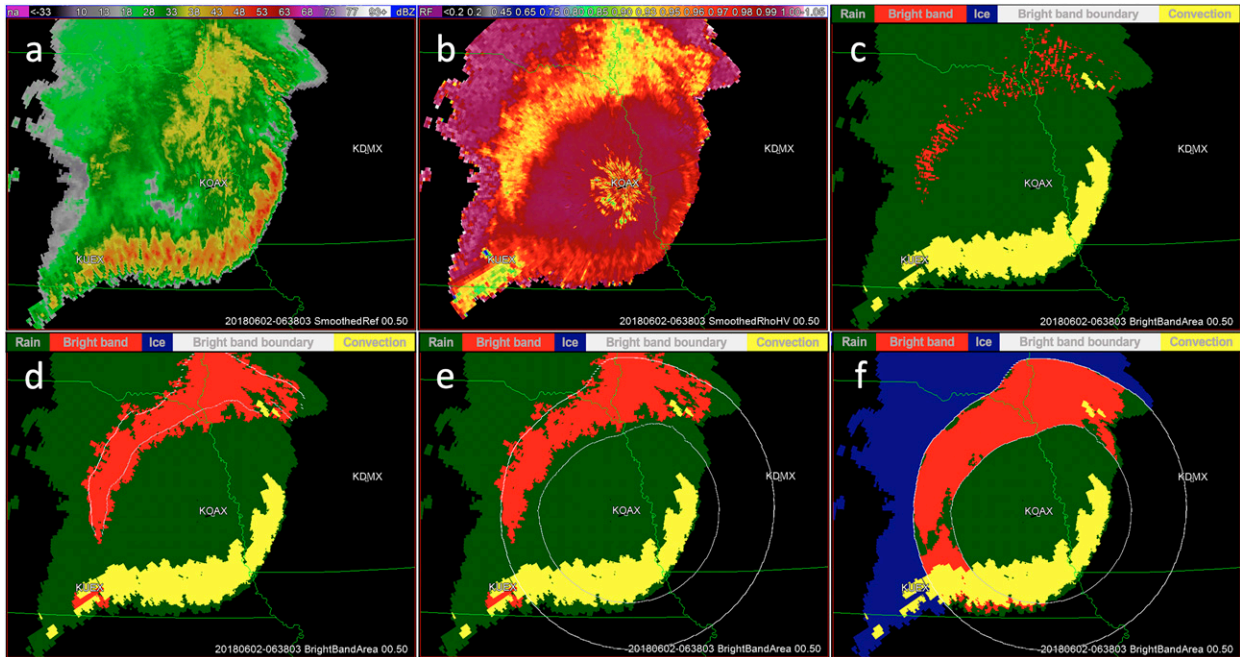
FIG. 2. (a) Smoothed reflectivity and (b) ρ_{hv} fields from KOAX at 0668 UTC 2 Jun 2018. (c) The high confidence BB gates (red pixels) and stratiform (green) convection (yellow) segregation output; (d) the BBA (red) after the seeded region growing and the 90/20 percentile top/bottom heights (white lines); (e) downward-shifted bottoms and 21° median filter smoothed and extrapolated BB top and bottom heights (white lines) to all 360° azimuth; and (f) the final convective (yellow) and stratiform (green) rain, BB (red), and ice (blue) regions.

reflectivity and ρ_{hv} fields, along with the output from the convection–stratiform segregation function.

b. Brightband area (BBA) delineation

This step delineates the brightband impacted area (BBA) on PPI (plan position indicator) scans of radar data, using a combination of preprocessed dual-pol variables, the High-Resolution Rapid Refresh (HRRR; Benjamin et al. 2016) model freezing level heights at the radar location, and the output of the convection–stratiform segregation. The BBA delineation only applies in the stratiform areas, starting at the highest tilt that might be used for QPE and works downward. The top-down approach allows for more accurate BB delineation due to higher vertical resolution and more prominent BB signatures in dual-pol data at increasing elevation angles (e.g., Giangrande et al. 2008). The BB heights from the higher tilts are then used to constrain the BB delineation on subsequent lower tilts, increasing the confidence in the latter where BB signatures can be obscured due to nonuniform beam filling, large beam widths at far ranges from the radar, and ground clutter.

On each tilt, the start and ending gates of the possible BBA are calculated for each radial using either the delineated BB top and bottom heights from the tilt above or a model freezing level height (FLH) otherwise. The height where the beam top (bottom) of a given radial intersects the BB bottom (top) delineated from the upper tilt are determined. These heights are then expanded by 250 m to ensure that the full extent of

the BBA can be captured, and the gates corresponding to these expanded heights define the start and end gates of the first guess BBA for the radial. The radial-by-radial calculation allows for the BB height to vary with azimuthal direction, no longer relying on the assumption of an isotropic melting layer across the radar domain.

The first guess BBA is searched for "high confidence" BB gates. The criteria for a gate being flagged as high confidence is listed in Table 1. A seeded region growing algorithm (Qi et al. 2013) is applied to capture the full BBA with the high confidence gates as the initial seeds. The criteria for the region growing are listed in Table 2. The values in Tables 1 and 2 were determined by analysis of multiple cases of varying BB height. Figure 2 shows an example reflectivity (Fig. 2a) and ρ_{HV} (Fig. 2b) fields from KOAX at 0638 UTC 2 June 2018 and the identified high confidence BB gates (red pixels, Fig. 2c). The BBA after the seeded region growing is shown in Fig. 2d.

Next, a reference BB top and bottom are determined for each radial. This is done by examining the BB gates (i.e., the red pixels in Fig. 2d) within a 21° azimuthal sector centered at a given radial. If the number of BB gates is greater than 100 within the sector, then the reference BB top (bottom) height is defined as the 90th (20th) percentiles of the BB gates within this 21° sector (see white lines in Fig. 2d). This step is similar to the methodology in Giangrande et al. (2008) and is applied to minimize potential contaminations from ground clutter near the radar and to assure a more representative BB top/bottom height. The reference BB

TABLE 1. Variable criteria for initial flagging of high-confidence brightband gates. Note that numbers in brackets are for low freezing levels and in parentheses are for tilt > 1.5°.

Variable	Min	Max
Z (dBZ)	30	60
ρ_{hv}	0.90, (0.85)	0.96, [0.97]
Std dev ρ_{hv}	0.008	0.02, [0.04], (0.06)
Std dev ϕ_{DP} (°)	1.0, (2.0)	4.0, (6.0)

TABLE 2. Variable ranges for seeded region growing for brightband expansion. Note that numbers in brackets are for low freezing levels.

Variable	Min	Max
Z (dBZ)	25	60
ρ_{hv}	0.80	0.97
Std dev ρ_{hv}	—	0.055, [0.08]
Std dev ϕ_{DP} (°)	—	8, [10]

bottom and top gates are then shifted toward and away from the radar, respectively, until no more contiguous BB gates exist to capture the full BB extent. A 21° median filter is applied next to ensure the azimuthal continuity of the delineated heights. Over small sectors where no BB was delineated, BB heights are linearly interpolated between the next identified BB gates to indicate the potential ML position. It was observed that there is often a slight offset between the gradient in ρ_{HV} and Z at the bottom of the BB due to nonuniform beam filling, or the required time it takes large newly melted liquid drops to fully break up. To account for this, the BB bottom gate is adjusted to where the beam top is completely below the BB bottom; a process that results in a shift toward the radar. These delineated heights are shown as the white lines in Fig. 2e.

If the FLH is less than 1 km and the BB bottom was determined to be very low, less than 250 m above radar level (ARL) on all delineated tilts thus far, then the BB bottom for the current tilt is shifted to be at the radar. This is done to prevent highly jagged BB bottom heights that appear typically due to the impacts of ground clutter surrounding the radar at the lowest elevation angles.

The final step of the BB delineation is to identify the reflectivity gates which do and do not need a reflectivity correction. All gates flagged as convection will not receive a reflectivity correction. Gates below the delineated BB bottom are flagged as stratiform rain not in need of a reflectivity correction. All gates above the delineated BB top are flagged as ice region, needing correction for overshooting. If no delineated heights exist for the radial, then the total average of the delineated heights is used for the bottom and top heights. Reflectivity gates not flagged as BB earlier will be flagged as stratiform rain not in need of a reflectivity correction. These final flags (Fig. 2f) determine which reflectivity gates receive a reflectivity correction outlined later in this section.

c. Construction of an azimuthally dependent dual-pol vertical profile of reflectivity

The term dpVPR refers to two different apparent vertical profiles that are used to calculate the final reference VPR for reflectivity corrections—one of Z and one of ρ_{HV}. The two apparent profiles are calculated for each of predefined sectors by taking azimuthal average of Z and ρ_{HV} within (red in Fig. 2f) and above (blue in Fig. 2f) the BBA as well as in the rain area (green in Fig. 2f) that is within 250-m height of the BBA. The sectors are 30° wide centered at the

nominal radials at 0°, 15°, 30°, …, 330°, and 345° azimuth. Case studies showed that the 30° window allows for enough data to calculate a stable, yet localized apparent vertical profile, as well as provides overlap between adjacent dpVPRs to limit discontinuities for reflectivity corrections. Figure 3 shows an example of the apparent vertical profiles of Z (black dotted line) and ρ_{HV} (red dotted line).

The BB peak is identified by finding the maximum Z that is also an inflection point in the Z profile. If this value is above 30 dBZ, it is identified as Z_{peak}. The height of this peak is H_{peak}. If no valid point is found, the region is again searched for simply the maximum in Z. Profiles with a maximum Z below 30 dBZ will be excluded for dpVPR correction. The inflection point methodology was selected first due to the typical reflectivity structure of the BB (Fabry and Zawadzki 1995). However, a very low and partly observed BB may have the Z peak occurring at the radar. In such instances, there will be no inflection point in the Z profile at the observed peak, so no inflection point is required during a second pass when identifying a Z peak to account for these situations.

The BB bottom height H_{bottom} is determined next with a first guess to be the average BB bottom height in the sector h_B. If this height in the dpVPR has $\rho_{HV} > 0.98$, $Z > 27.5$ dBZ,
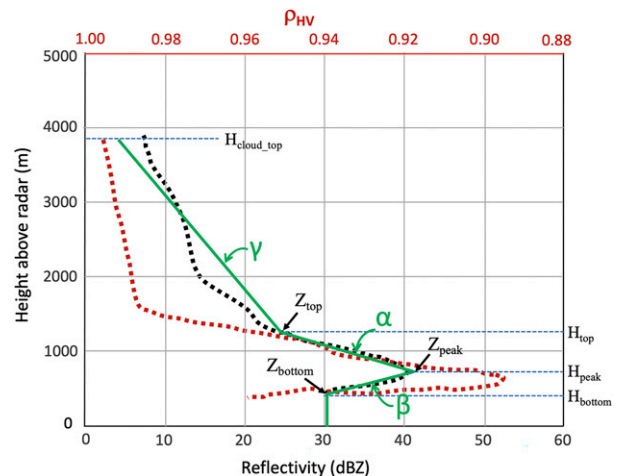

FIG. 3. An example of apparent vertical profiles of Z (black dotted line) and ρ_{HV} (red dotted line) and the linearly fitted dpVPR model (green line). The BB bottom, peak, and top heights and reflectivity parameters (H_{bottom}, Z_{bottom}, H_{peak}, Z_{peak}, H_{top}, Z_{top}), the cloud top height (H_{cloud_top}), and the slopes (α, β, γ) associated with the linear dpVPR are marked. Detailed discussions can be found in the text.

TABLE 3. Single radar case study events used in this study.

Case No.	Ending time/date of the 24-h period	Radar	Description of the BB event
1	1500 UTC 20 Feb 2017	KRTX (Portland, OR)	Light stratiform rain with low, nonisotropic BB
2	1100 UTC 14 May 2017	KBOX (Boston, MA)	Moderate stratiform rain with low, nonisotropic BB
3	1100 UTC 14 May 2017	KENX (Albany, NY)	Moderate stratiform rain with low, nonisotropic BB
4	1200 UTC 3 Mar 2018	KBOX (Boston, MA)	Moderate stratiform rain with low to very low, nonisotropic BB
5	1200 UTC 2 Jun 2018	KOAX (Omaha, NE)	MCS with BB in stratiform rain
6	1200 UTC 14 Apr 2019	KTLX (Norman, OK)	Moderate stratiform rain with low to very low, nonisotropic BB
7	1200 UTC 7 May 2019	KICT (Wichita, KS)	MCS with BB in stratiform rain
8	1200 UTC 7 May 2019	KTWX (Topeka, KS)	MCS with BB in stratiform rain
9	1200 UTC 7 May 2019	KUEX (Hastings, NE)	MCS with BB in stratiform rain
10	1300 UTC 14 Dec 2020	KHPX (Hopkinsville, KY)	Moderate stratiform rain with very low, nonisotropic BB
11	1300 UTC 14 Dec 2020	KJKL (Jackson, KY)	Light stratiform rain with very low, nonisotropic BB
12	1300 UTC 14 Dec 2020	KOHX (Nashville, TN)	Moderate stratiform rain with very low, nonisotropic BB
13	1300 UTC 14 Dec 2020	KSRX (Fort Smith, AR)	Light stratiform rain with very low, nonisotropic BB
14	1200 UTC 25 Mar 2021	KDDC (Dodge City, KS)	Light stratiform rain with very low, nonisotropic BB

and is located at least 250 m below H_{peak}, it is saved as H_{bottom}. If these conditions are not met, the dpVPR is searched downward, then upward, until they are met. The gate where these conditions are first met is flagged as H_{bottom}. If this still fails to satisfy the criteria, then h_B is kept as H_{bottom}, but is flagged as suspect for later investigation.

Last, the BB top height H_{top} is determined with the average BB top in the sector, h_T as the first guess. If $Z(h_T) > 25$ dBZ, $Z_{\text{peak}} - Z(h_T) < 15$ dBZ, and h_T is at least 250 m above H_{peak}, it is kept as H_{top}. If these conditions are not met, the dpVPR is first searched downward, then upward until these conditions are met. The ρ_{HV} is not examined when determining the BB top due to small ρ_{HV} gradient near the BB top especially at far ranges from the radar, or on the edge of the precipitation system.

Once H_{peak}, H_{bottom}, and H_{top} have been identified, linear regression is performed to the dpVPR and three slopes (green lines, Fig. 3) are calculated. The slope β represents the segment between H_{bottom} and H_{peak}; α, the segment between H_{peak} and H_{top}; and γ, the segment between H_{top} and $H_{\text{cloud\_top}}$, where cloud top is the highest valid reflectivity in the dpVPR (Fig. 3). After these linear fits are calculated, H_{bottom} and β are checked for potentially low and incomplete BB observation. This condition occurs when H_{bottom} is at the radar, indicating that the BB is likely not fully observed by the radar. Under this condition, if β is determined valid ($H_{\text{peak}} > 250$ m ARL, and $Z_{\text{peak}} - Z_{\text{bottom}} > 3$ dBZ), then a new H_{bottom} is calculated to be where a reference Z_{bottom} is reached, which is a function of Z_{peak}. Otherwise, β is reset to $-\alpha$ assuming a symmetrical BB with respect to the peak (Fabry and Zawadzki 1995; Qi et al. 2012), and a new H_{bottom} is calculated using the reference Z_{bottom}. If $Z_{\text{peak}} - Z_{\text{bottom}} < 5$ dBZ or $H_{\text{peak}} - H_{\text{bottom}} < 250$ m then the linear fit for β is considered low confidence due to insufficient data samples, and β will be reset to be $-\alpha$. Last, if H_{bottom} was flagged as suspect (as described prior) but β passed the validity check conditions, then the value of β is kept, but H_{bottom} is recalculated using the reference Z_{bottom}. All three slopes are checked for an upper limit to ensure a physically realistic BB structure. If all of these sanity checks pass then the linear

fits are considered valid and this linear dpVPR will be used for reflectivity corrections, outlined in the following subsection.

d. Reflectivity corrections

Reflectivity within the BB and ice regions are corrected on each radial where a BB was identified. These reflectivity corrections are done using the closest two dpVPRs adjacent to the radial being corrected. Both dpVPRs will be used to calculate a final corrected reflectivity value to ensure azimuthal continuity in the corrected reflectivity field, using a weighted combination based on the relative position of the radial to the adjacent dpVPRs. The dpVPR weights w_1 and w_2 are

$$w_1 = \frac{|\text{azm}_{\text{obs}} - \text{azm}_{\text{norm1}}|}{|\text{azm}_{\text{norm2}} - \text{azm}_{\text{norm1}}|}, \tag{1a}$$

$$w_2 = 1.0 - \frac{|\text{azm}_{\text{obs}} - \text{azm}_{\text{norm2}}|}{|\text{azm}_{\text{norm2}} - \text{azm}_{\text{norm1}}|}. \tag{1b}$$

Here, azm_{obs}, $\text{azm}_{\text{norm1}}$, and $\text{azm}_{\text{norm2}}$ are azimuth angles (°) of the given radial for correction and the two adjacent nominal radials, respectively. Note that $|\text{azm}_{\text{norm2}} - \text{azm}_{\text{norm1}}| = 15°$ is the azimuthal interval between the nominal dpVPR radials used in this study. Only the gates that were flagged as BB or ice by the BB delineation algorithm (Fig. 2f) will receive a reflectivity correction. The final corrected reflectivity Z_{corr} is calculated as

$$Z_{\text{corr}}(h) = Z_{\text{obs}}(h) + w_1 \Delta Z_{\text{corr1}} + w_2 \Delta Z_{\text{corr2}}. \tag{2}$$

Here, h is the height of the given gate for correction; Z_{obs} and Z_{corr} are observed and corrected reflectivities (dBZ); ΔZ_{corr1} and ΔZ_{corr2} are reflectivity differences between the height h and the BB bottom in the two adjacent dpVPRs, respectively.

Reflectivity corrections within the ice region are capped at 35 dBZ to avoid potential "runaway" corrections at far ranges. Such unphysical corrections may occur where the beam intersects
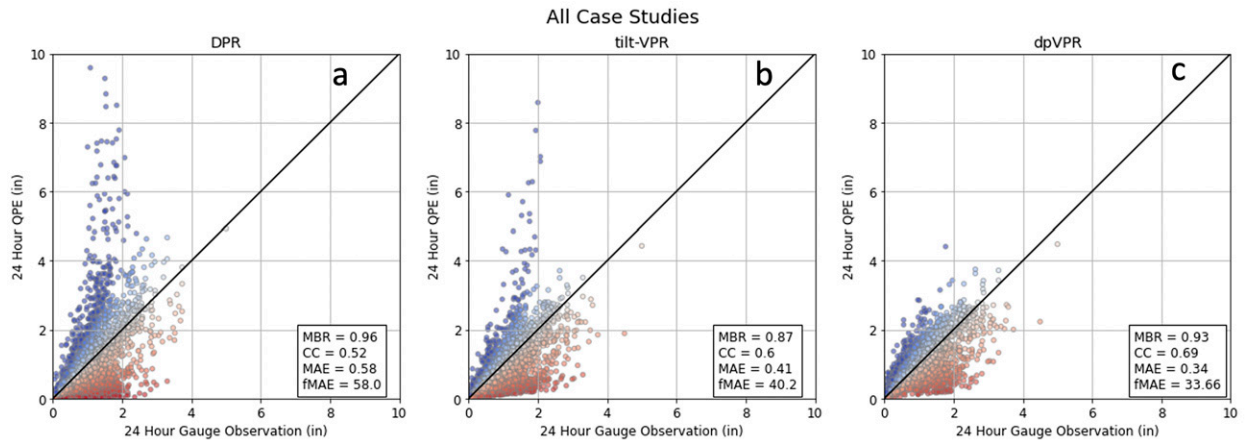
FIG. 4. Radar QPEs with (a) the DPR, (b) the Zhang and Qi (2010) tilt-VPR correction, and (c) the new dual-pol VPR correction vs CoCoRaHS gauges for all the cases listed in Table 3.

a second and higher-level melting layer or enters the upper part of a weak and unidentified convective area at far ranges. Reflectivities greater than 35 dBZ in the ice region receive no correction.

While the current dpVPR scheme assumes a "single peak" bright bead structure, it does not necessarily assume a uniform melting layer along the radial. Rather, the apparent vertical profiles and the linear model can be a bulk result of a melting layer that slowly changes its height with range. Using the "apparent" profiles based on the real-time data, the current scheme tries to correct for the bulk effect of the melting layer along the range. However, if the bulk effect of the melting layer on the apparent radial profiles of reflectivity and correlation coefficient results in multiple peaks (e.g., two melting layers at different heights), the current methods may not provide an accurate correction.
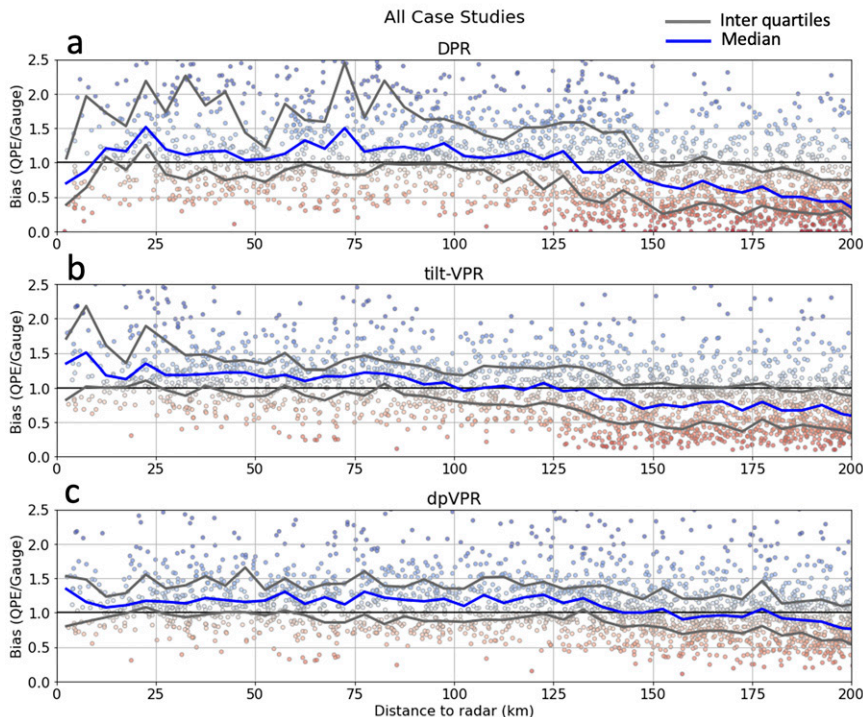
FIG. 5. Distance to radar (km) vs mean bias ratio for each QPE–gauge pair for all the case studies in Table 3 with (a) the DPR, (b) tilt-VPR, and (c) dpVPR. Blue (gray) lines represent the median (inter quartile range) for each 5-km range interval.
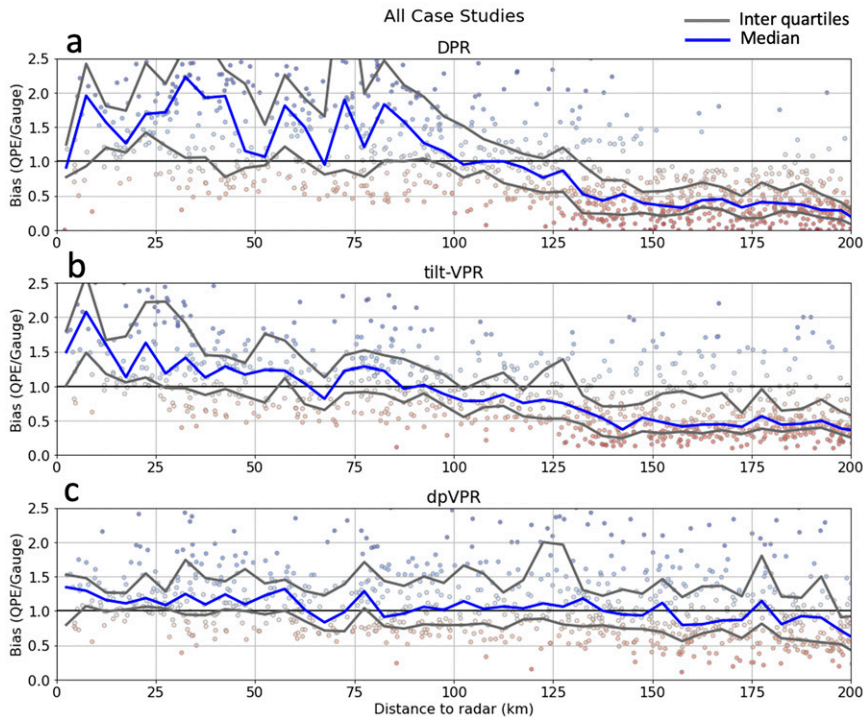
FIG. 6. As in Fig. 5, but for all the cases in November–March.

3. Results

The dpVPR correction scheme was tested for 14 cases from different locations across the CONUS that had varying degrees of BB heights, intensities, and symmetry (Table 3). For all case studies, 24-h QPE was calculated using Z–R relationships of $Z = 75R^2$ and $Z = 300R^{1.4}$ for stratiform and convection (Zhang et al. 2016), respectively, and validated using 24-h CoCoRaHS (Community Collaborative Rain, Hail and Snow Network, www.cocorahs.org; Cifelli et al. 2005) gauge observations. The manual CoCoRaHS observations were chosen for the quantitative evaluations for all cases due to their higher accuracy and robustness than the automated hourly gauges, which are prone to issues including partial or full clogging, instrumentation malfunctions, etc. Nevertheless, hourly gauges from the Meteorological Assimilation Data Ingest System (MADIS; Miller et al. 2007; Helms et al. 2009) were used in a couple of detailed case studies to help understand the dynamic
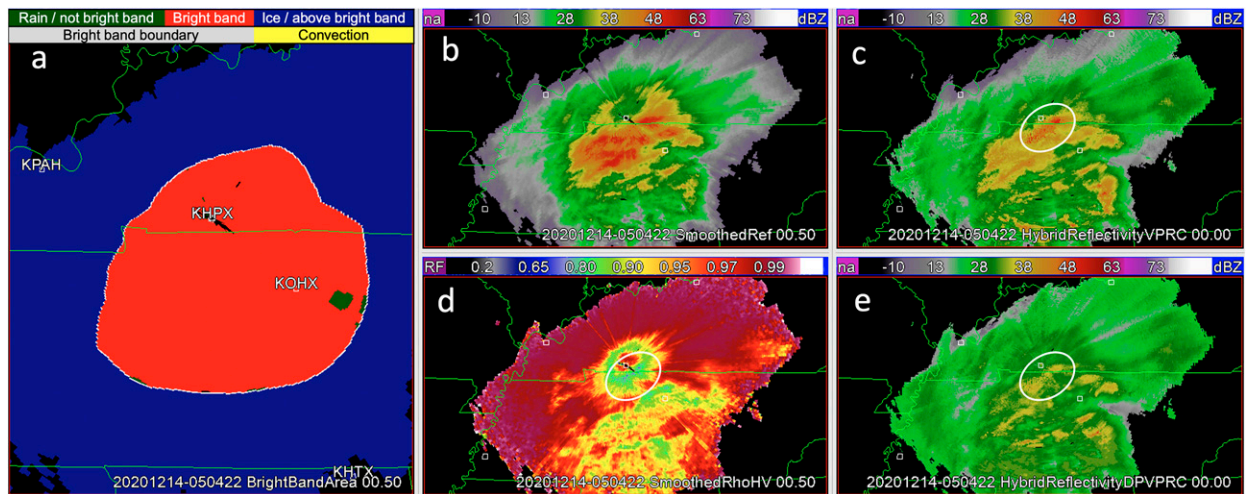

FIG. 7. (a) Delineated brightband area, (b) smoothed reflectivity, (c) tilt-VPR corrected reflectivity, (d) smoothed ρ_{hv}, and (e) dpVPR corrected reflectivity at KHPX at 0504 UTC 14 Dec 2020.
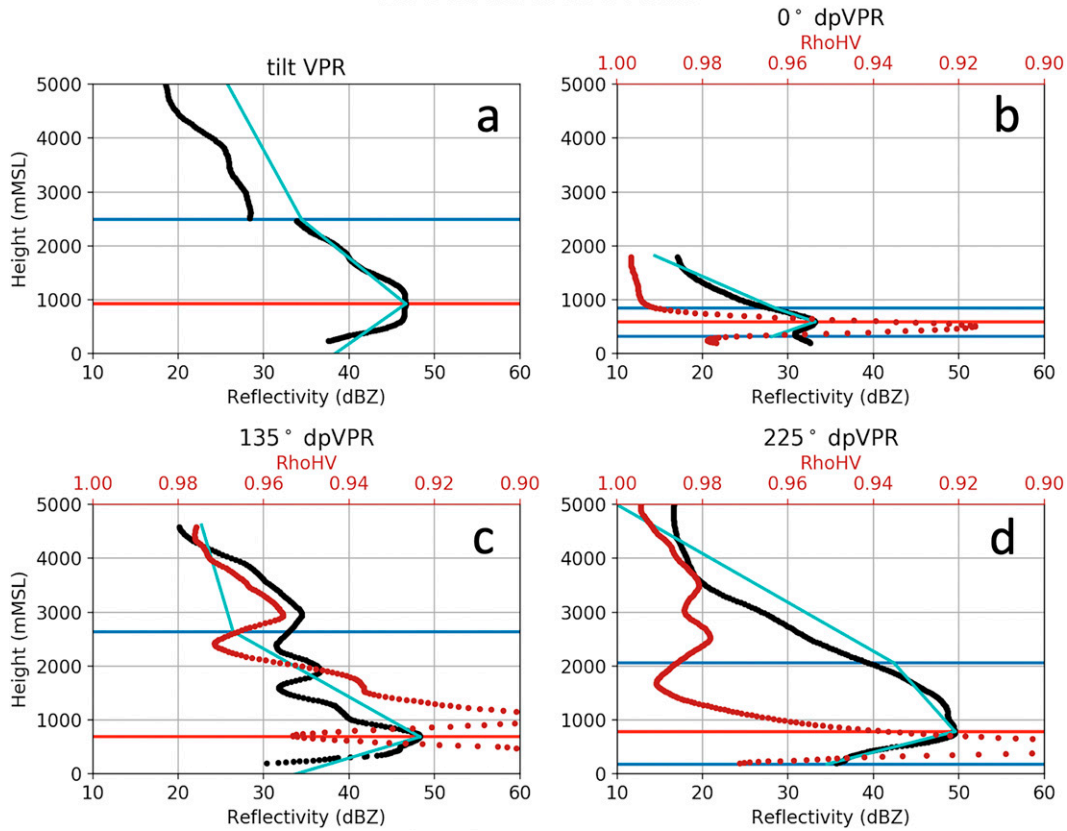
FIG. 8. (a) The tilt-VPR and the new dpVPRs at azimuths (b) 0, (c) 135, and (d) 225. Black lines represent the reflectivity profile, red dots the ρ_{hv} profile, red horizontal line the BB peak, blue horizontal lines the BB top and bottom, and cyan lines the linear fits of the VPR.

brightband impacts on the radar QPEs qualitatively. Note that the CoCoRaHS observations are obtained at a nominal time of 0700 local time. Therefore, the number of reports changes with the regions and seasons and usually peaks around 1100 UTC on the East Coast of the United States in the warm season and 1500 UTC on the West Coast in the cool season. The 24-h QPE time windows (Table 3) were different for different cases to capture the most gauge data.

Figure 4 shows scatterplots of the gauges versus the radar QPEs with the DPR (Fig. 4a), tilt-VPR correction (Fig. 4b) and with the new dpVPR correction (Fig. 4c) for all of the 14 cases. The four statistic scores in Fig. 4 are defined as follows:

mean bias ratio (MBR)

$$MBR = \overline{Q}/\overline{G}, \qquad (3)$$

$$\overline{Q} = \frac{\sum\limits_{i=1}^{N} Q_i}{N}, \qquad (3a)$$

$$\overline{G} = \frac{\sum\limits_{i=1}^{N} G_i}{N}, \qquad (3b)$$

correlation coefficient (CC)

$$CC = \frac{\sum\limits_{i=1}^{N}(Q_i - \overline{Q})(G_i - \overline{G})}{\sqrt{\sum\limits_{i=1}^{N}(Q_i - \overline{Q})^2 \sum\limits_{i=1}^{N}(G_i - \overline{G})^2}}, \qquad (4)$$

mean absolute error (MAE)

$$MAE = \frac{1}{N}\sum\limits_{i=0}^{N}|Q_i - G_i|, \quad \text{and} \qquad (5)$$

fractional MAE (fMAE)

$$fMAE = 100 \times MAE/\overline{G}, \qquad (6)$$

where N is the total number of QPE–gauge pairs for the given dataset, Q_i and G_i are the radar estimated and gauge observed 24-h rainfalls at the ith gauge, respectively.

The DPR QPE (Fig. 4a) had large scatters compared to the CoCoRaHS gauges with a MAE of 0.58 in. and fMAE of 58%. The overall bias was ~4% underestimation but there were significant local over- and underestimations. Figure 5
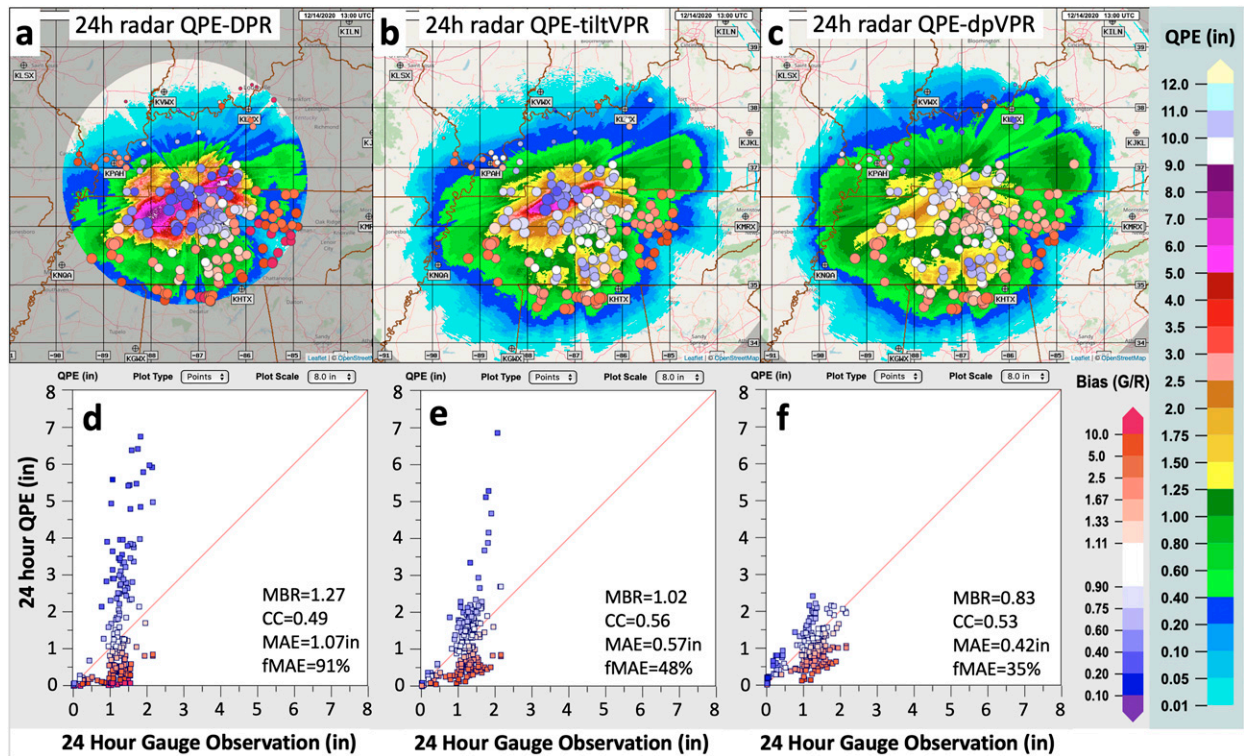
FIG. 9. KHPX 24-h QPEs ending at 1300 UTC 14 Dec 2020 from (a) DPR, (b) the tilt-VPR, and (c) the dpVPR corrections, and their scatterplots vs gauges from (d) DPR, (e) tilt-VPR, and (f) dpVPR. The colored dots in (a)–(c) represent gauge sites, the size of the dots represent the gauge amounts, and color represents the gauge/QPE bias ratios. Cool dot colors (blues) indicate overestimation, and warm colors (red or pink) indicate underestimation.

shows the MBRs of the DPR, tilt-VPR, and dpVPR as a function of range. The DPR QPE had very large scattering compared to gauges with overestimations at close ranges and underestimation at far ranges (Fig. 5a), even though a rate correction was applied to mitigate VPR effects within and above the BB (Giangrande and Ryzhkov 2008). The correction applies constant multipliers to the rate field based on the hydrometeor classification algorithm (HCA; Park et al. 2009). In areas of wet snow and graupel, a 0.6 and 0.8 multiplier were applied to the rate, respectively. In areas of rain/hail mix beyond the range (R_t in Giangrande and Ryzhkov 2008) where the radar beam fully overshoots the BB, a 0.8 multiplier was applied. These are to mitigate potential overestimations in the radar QPE associated with the bright band. In areas of snow and ice crystal beyond R_t, a 2.8 multiplier was applied to mitigate potential underestimation associated with radar beam overshooting the melting layer. Detailed case analysis later in this section indicated that the HCA and BB top delineation might have had challenges handling the very low and intense bright bands and thus the large errors.

The tilt-VPR QPE (Fig. 4b) reduced the majority of the overestimation compared to the DPR (Fig. 4a), but with a small number of overestimations that mainly from events with a low bright band. Such bright bands tend to be intense and sometimes highly inhomogeneous, which pose a challenge to the tilt-VPR that is based on reflectivity field only and

assumes a uniform BB structure across the domain. Figure 5b showed significant overestimation bias in the tilt-VPR QPE at ranges within 30 km, indicating some low BBs were not fully corrected. Meanwhile, the tilt-VPR mitigated the underestimation and significantly tightened the scatter (Figs. 4b and 5b). The overall bias was a 13% underestimation in the tilt-VPR QPE and the CC score was increased from 0.47 in. the DPR QPE to 0.60 and MAE (fMAE) was reduced from 0.73 in. (73%) to 0.41 in. (40%).

The new dpVPR correction eliminated the residual overestimation in the tilt-VPR and further tightened the scatter compared to the gauges (Figs. 4c and 5c versus Figs. 4b and 5b). The underestimation bias was reduced from 13% to 6%, the CC score increased from 0.60 to 0.69, and the MAE was reduced from 0.41 to 0.34 in., a reduction of ~16%. The improved mitigation of the overestimation errors in the dpVPR QPE (Fig. 4c) was a result of the better delineation of BB areas using the dual-pol variables. Further, the azimuthally variant dpVPRs captured local VPR slopes better than the domain averaged tilt-VPR and the constant multipliers in the DPR, especially in the ice region, providing more accurate reflectivity corrections at far ranges and resulted in less underestimation. Within 30 km from the radar, the dpVPR QPE had a median bias ratio (blue line) closer to 1.0 than in the DPR and tilt-VPR and the MBR spread was reduced from ~0.85 in the tilt-VPR (Fig. 5b) to ~0.5 in the dpVPR (Fig. 5c), showing
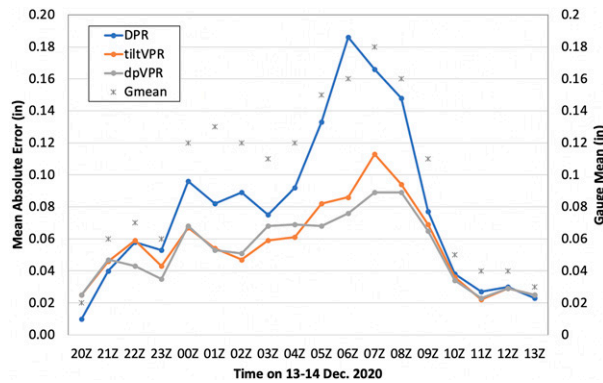
FIG. 10. Time series of MAEs of the hourly DPR (blue line), tilt-VPR (orange line), and dpVPR (gray line) QPEs vs MADIS gauges from 2000 UTC 13 Dec to 1300 UTC 14 Dec 2020. The gray stars represent the domain mean hourly gauge amounts.

advantages of the dpVPR in handling low BBs. Between 30 and 140 km, the tilt-VPR performed similarly to the dpVPR. After 140 km, the median MBR of the tilt-VPR QPE dropped below 1 rapidly (Fig. 5b) indicating the underestimation due to beam overshooting the melting layer. With the dpVPR methodology, this range is extended to ~180 km (Fig. 5c) and the MBR spread beyond 125 km was reduced to ~0.5 from ~0.7 in the tilt-VPR. The tilt-VPR did not provide effective reflectivity corrections at far ranges due to the 360° average of the reference VPR not capturing the local slopes in the ice region. The underestimation issue is even more pronounced in cool season where stratiform precipitation with low melting layers and cloud tops are more prevalent. Figure 6 shows the MBR of the three QPEs for all cases in the November–March months and the underestimation bias in the tilt-VPR (Fig. 6b) was apparent starting at the range of ~90 km. The dpVPR, on the other hand, maintained an overall bias-free estimate up to ~180 km (Fig. 6c).

To further illustrate the strengths and limitations of the current methodology with respect to the two reference QPEs, a detailed analysis of selected cases is presented next.

a. KHPX 14 December 2020

Figure 7 shows the BBA output, smoothed reflectivity, smoothed ρ_{hv}, tilt-VPR, and dpVPR corrected reflectivity for an event characterized by a very low, highly nonisotropic BB event. At the time illustrated in Fig. 7, the BB was strongest and deepest to the south and east of KHPX, with reflectivity intensities reaching upward of 50 dBZ (Fig. 7b). To the north of the radar, the BB was weaker with reflectivity intensities reaching only 35 dBZ (Fig. 8b). This nonisotropic BB resulted in a tilt-VPR with a moderately strong BB ($Z_{peak} \approx 47$ dBZ and $Z_{peak} - Z_{bottom} \approx 8$ dBZ, Fig. 8a). The dpVPRs, on the other hand, illustrated the significantly different BB structure in different azimuthal directions. The dpVPR at radial zero (Fig. 8b) showed a shallow BB with a peak intensity of 33 dBZ, while the dpVPR at radials 135 and 225 (Figs. 8c,d) showed a very deep BB ($Z_{peak} - Z_{bottom} \approx 14$–15 dB$Z$) with a peak intensity of 48–50 dBZ. These dpVPRs are more representative of the varying intensity and structure across the radar domain and the dpVPR corrected reflectivity field (Fig. 7e) appeared to have less BB contamination than was the tilt-VPR corrected reflectivity (Fig. 7c).

QPEs from the DPR and the tilt-VPR and dpVPR corrected reflectivity fields illustrate a few stark differences (Fig. 9). DPR QPE had very large overestimations near the radar (blue dots in Fig. 9a) and underestimations near the edge of the domain (red dots in Fig. 9a). The large errors were also reflected in the scatterplot versus CoCoRaHS gauges (Fig. 9d). As a result, the MAE was 1.07 in. and fMAE was 91%. A time series of the hourly MAEs of the three QPEs is shown in Fig. 10, which shows the largest DPR errors during 0500–0800 UTC 14 December 2022. A closer look at the hourly QPE map at 0700 UTC 14 December 2022 compared to gauges (Fig. 11a) revealed an area of large overestimations near the radar (white circle, Fig. 11a), similar to those in the 24-h DPR QPE. The overestimation occurred in areas of very intense reflectivities (Fig. 11b) that were classified as rain/hail mix (red area in Fig. 11c). Since the rain/hail area was within the range of R_t (the dashed black circle, Figs. 11a,c), no correction multiplier was applied to the rates (Giangrande and Ryzhkov 2008) and thus the overestimation. This issue was also documented in a study by Cocks et al. 2016.
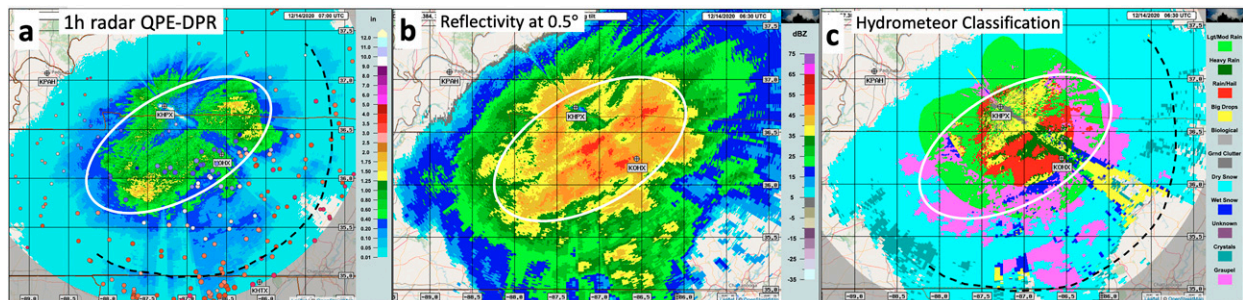

FIG. 11. (a) Hourly DPR QPE ending at 0700 UTC 14 Dec 2020, (b) the 0.5° tilt reflectivity, and (c) the hydrometeor classification at 0630 UTC 14 Dec 2020. The white circles indicate an area of large overestimation in the DPR QPE due to inaccurate melting layer delineation and hydrometeor classification. The black dashed circle indicates the range R_t in Giangrande and Ryzhkov (2008) beyond which the rain/hail mixed pixels [red area in (c)] will receive a correction.
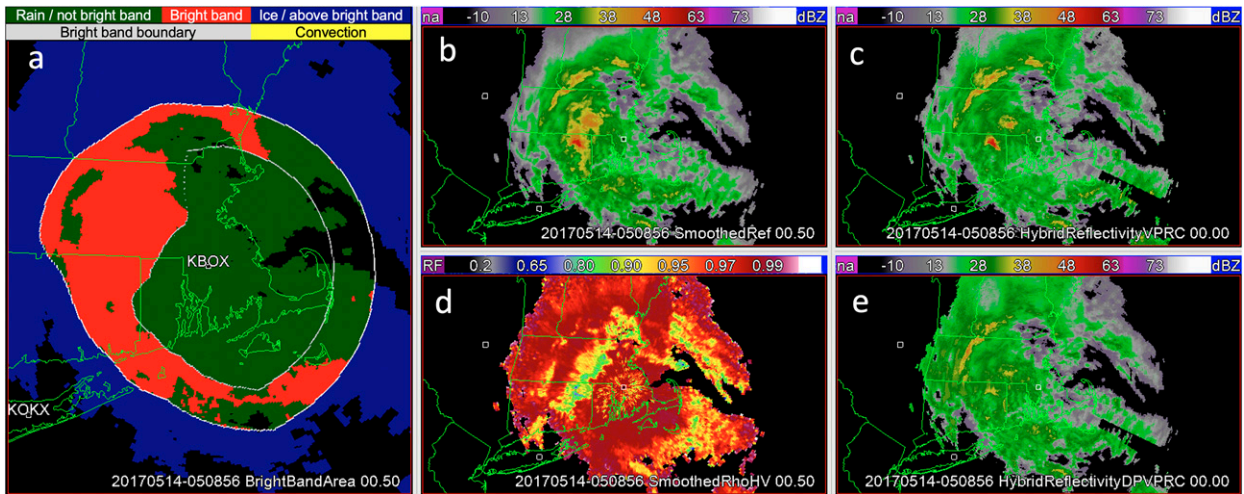
FIG. 12. (a) Delineated brightband area, (b) smoothed reflectivity, (c) ZQ10 tilt-VPR corrected reflectivity, (d) smoothed ρ_{hv}, and (e) dpVPR corrected reflectivity at KBOX at 0508 UTC 14 May 2017.

Tilt-VPR QPE in this case also had significant overestimation near the radar (Figs. 9b,e) but to a lesser extent than the DPR. The overestimation was due to the reflectivity field not receiving enough of a melting layer correction (Fig. 7c). The insufficient corrections are due to two factors: 1) the nonisotropic BB resulting in a tilt-VPR with an unrepresentative weaker peak reflectivity compared to the most intense band of

higher reflectivity, and 2) a constraint based on the vertically integrated liquid (VIL) when applying a reflectivity correction. The VIL constraint was applied to avoid a VPR correction in convective rain areas. However, VIL values in very intense BB can reach levels similar to those in weak convection, thus preventing a reflectivity correction from being applied (white circle, Fig. 7c). The domain mean bias did not reflect the
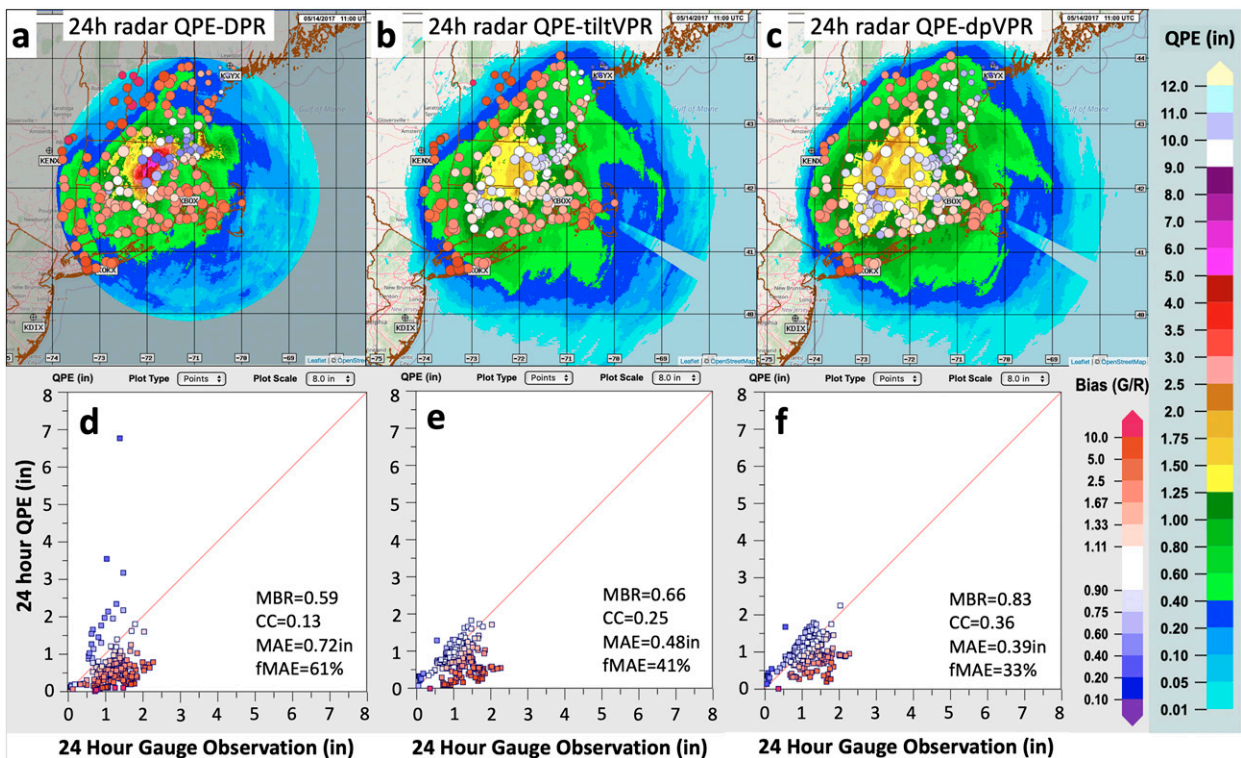

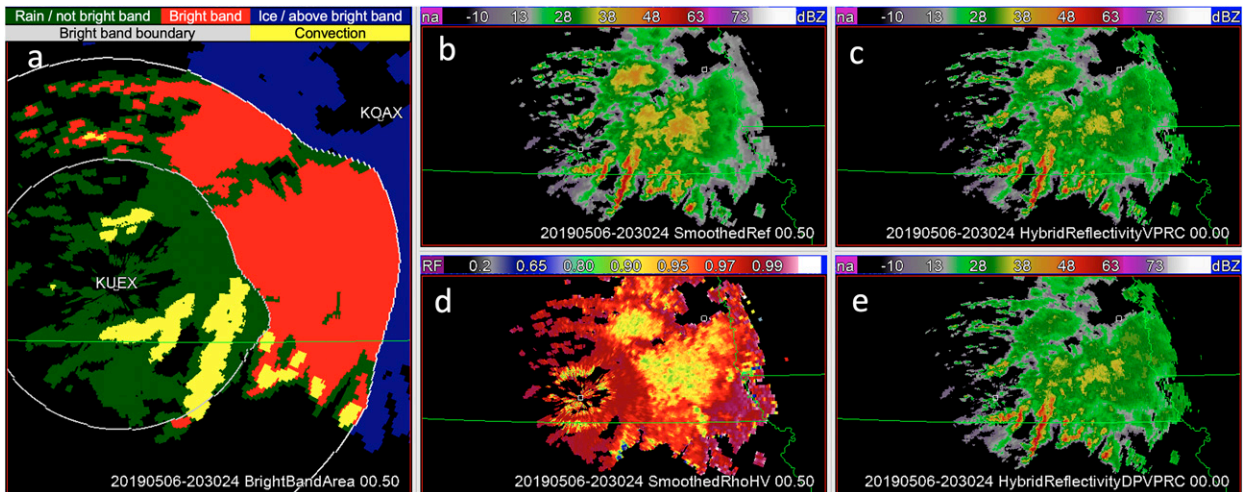FIG. 13. As in Fig. 9, but for KBOX radar at 1100 UTC 14 May 2017.

FIG. 14. (a) Delineated brightband area, (b) smoothed reflectivity, (c) tilt-VPR corrected reflectivity, (d) smoothed ρ_{hv}, and (e) dpVPR corrected reflectivity at KUEX at 2030 UTC 6 May 2019.

overestimation near the radar due to the underestimation at far ranges. The MAE was 0.57 in. and fMAE was 48% (Fig. 9e), both an improvement from the DPR.

The dpVPR QPE (Fig. 9c) eliminated the overestimation near the radar and further reduced the MAE from 0.57 to 0.42 in. and the fMAE from 48% to 35%. The use of ρ_{HV} to delineate BBA in the dpVPR reduced mistreatments of

intense BB as convections (white circles Figs. 7d,e). The azimuthally varying dpVPR better captures the localized BB intensities, resulting in a more effective reflectivity correction (Fig. 7e) and a QPE that was in much better agreement with the gauges. There was still a dry bias at very far ranges in all three QPE fields where the beam overshooting effect was too severe to be corrected. However, those
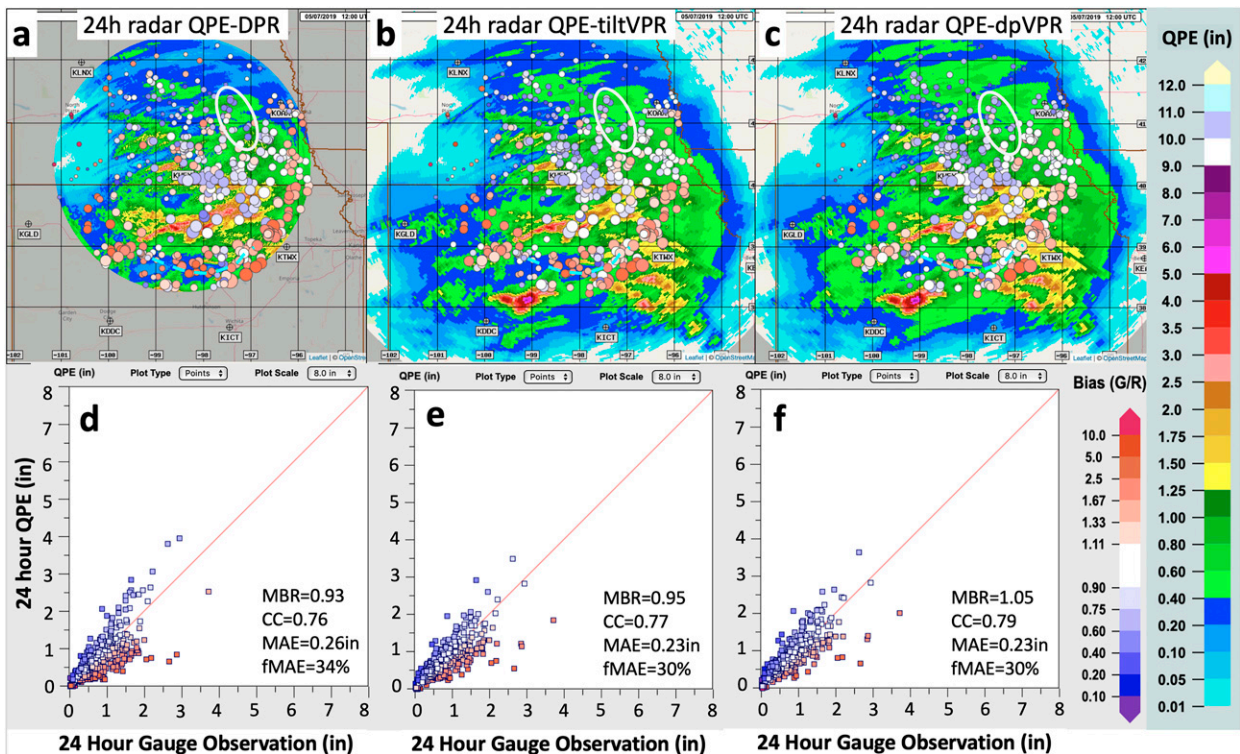

FIG. 15. As in Fig. 9, but for KUEX radar at 1200 UTC 7 May 2019. The white circle indicates an area of DPR QPE overestimation, and the cyan dashed line an area of underestimation in DPR and tilt-VPR QPEs.
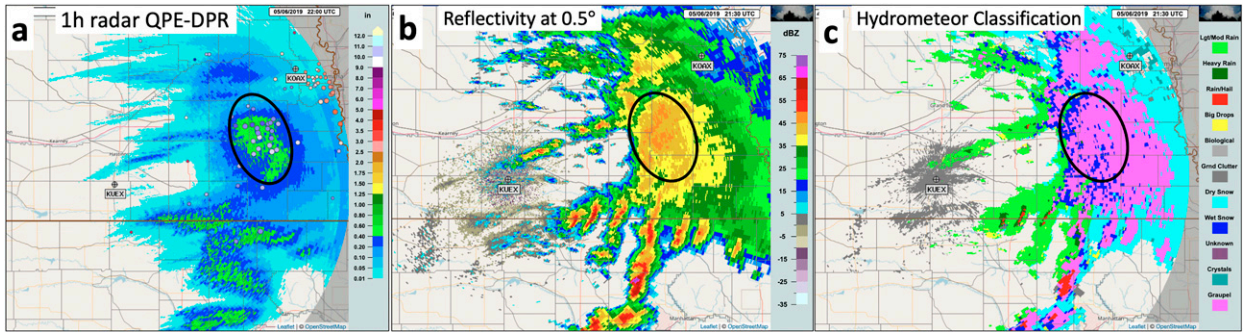
FIG. 16. (a) Hourly DPR QPE ending at 2200 UTC 6 May 2019, (b) the 0.5° tilt reflectivity, and (c) the hydrometeor classification at 2130 UTC 5 May 2019. The black circles indicate an area of DPR QPE overestimation due to insufficient correction to the rate for the brightband effect. The area was correctly identified as mostly graupel [pink in (c)] and received a correction with a multiplier of 0.8.

areas will likely be replaced with QPEs from neighboring radars that have closer range observations with better dpVPR corrections.

b. KBOX 14 May 2017

Figure 12 shows another nonisotropic BB event occurring around KBOX. The BB was consistently stronger and deeper to the west of KBOX, and most of the BBA was successfully captured despite the precipitation being noncontiguous (Fig. 12a). The dpVPR was able to capture the nonisotropic BB well, resulting in a corrected reflectivity field that was

continuous across the radar domain (Fig. 12e). The tilt-VPR methodology, on the other hand, over corrected reflectivities in the rain areas south of the radar (Fig. 12c), and did not apply enough correction where the BB is strongest. Also due to the reliance on VIL thresholds, the strongest region of the BB directly west of KBOX did not receive reflectivity corrections (Fig. 12c). The 24-h DPR QPE (Figs. 13a,d) again had the largest errors among the three products due to the challenges it had with low and intense bright band. The 24-h QPE for the tilt-VPR had underestimations nearest the radar, extending to the southwest (Fig. 13b). The underestimations at further ranges in the ice region of precipitation were not effectively
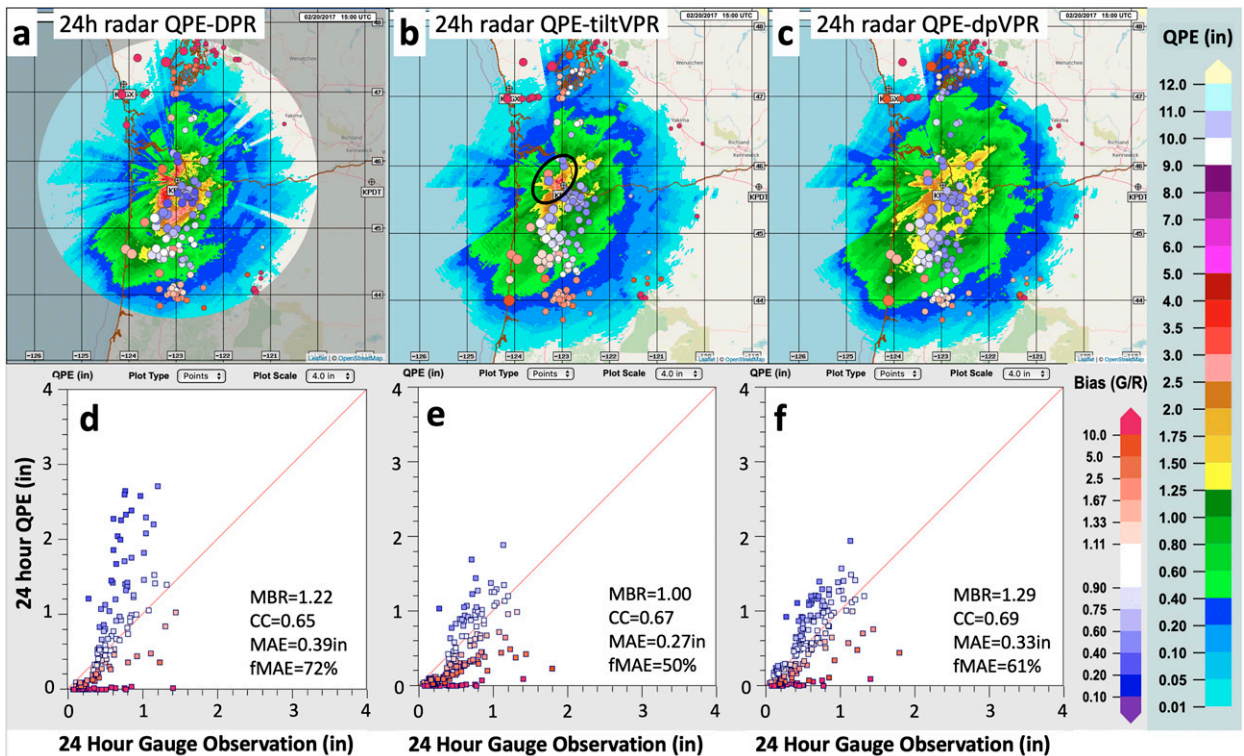

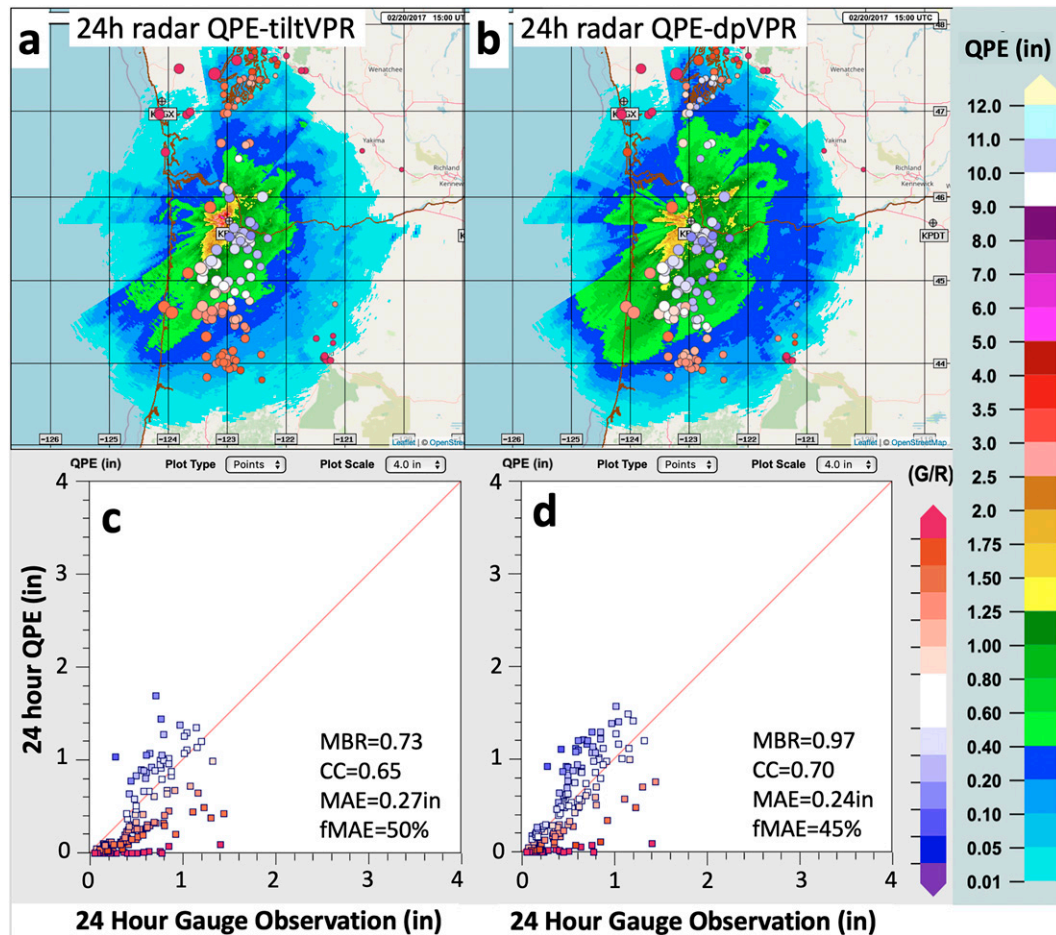FIG. 17. As in Fig. 9, but for KRTX at 1500 UTC 7 Feb 2017.

FIG. 18. As in Figs. 17b,c,e,f, but using the $Z = 210R^{1.46}$ relationship.

corrected due to the domain-average VPR not capturing reflectivity slopes. With the dpVPR (Figs. 13c,f), the dry bias was reduced by 17% (bias ratio increased from 0.66 to 0.83) and the MAE was reduced by ~19% (from 0.48 to 0.39 in.).

c. KUEX 7 May 2019

This event was characterized by convection and stratiform rain initially, transitioning to a mesoscale convective system (MCS) with a trailing stratiform precipitation region. During the period of broken convection, the BB was fairly uniform in height and intensity (Fig. 14). This BB was captured well by the tilt-VPR, which also successfully delineated the areas of convection. Warm-season, isotropic BB are handled well by the tilt-VPR methodology, and as such, the corrected reflectivity (Fig. 14c) appears to be reasonable. The use of the dpVPR does not result in many changes to the corrected reflectivity field (Fig. 14e versus Fig. 14c), indicating that situations where the tilt-VPR methodology works will not be degraded by the dpVPR. The DPR, tilt-VPR, and dpVPR QPE fields are very similar (Fig. 15) with two small differences, one to the northeast of KUEX where DPR QPE had a slightly more overestimation (white circles, Fig. 15) and another in the ice region at far ranges south of KUEX where DPR and tilt-VPR QPEs

had a slightly more underestimation (cyan dashed lines, Fig. 15). A closer look at the hourly DPR QPE map (Fig. 16a) at 2200 UTC 6 May 2020, the base reflectivity (Fig. 16b) and the hydrometeor classification (Fig. 16c) indicated that the overestimation in DPR was likely due to insufficient correction to the rate in the area of graupel (multiplier = 0.8). Overall, the DPR and tilt-VPR QPEs had slight underestimation bias of 7 and 5%, respectively, and the dpVPR has a slight overestimation of 5%. The DPR had a slightly larger MAE of 0.26 in. than the tilt-VPR and dpVPR QPEs, both of which had 0.23 in.

d. KRTX 20 February 2017

On 20 February 2017, a very low and nonisotropic BB event characterized by periods of contiguous and broken precipitation was observed around KRTX. Precipitation was light to moderate with this event, with most 24-h gauge totals measuring under 1 in. of rain (Fig. 17). The 24-h DPR QPE (Figs. 17a,d) again had an overestimation near the radar for this low brightband event and resulted in the largest MAE error of 0.39 in. among the three QPEs. The tilt-VPR methodology was able to apply an adequate reflectivity correction for most of the event, however, regions to the west of the radar did not always receive a
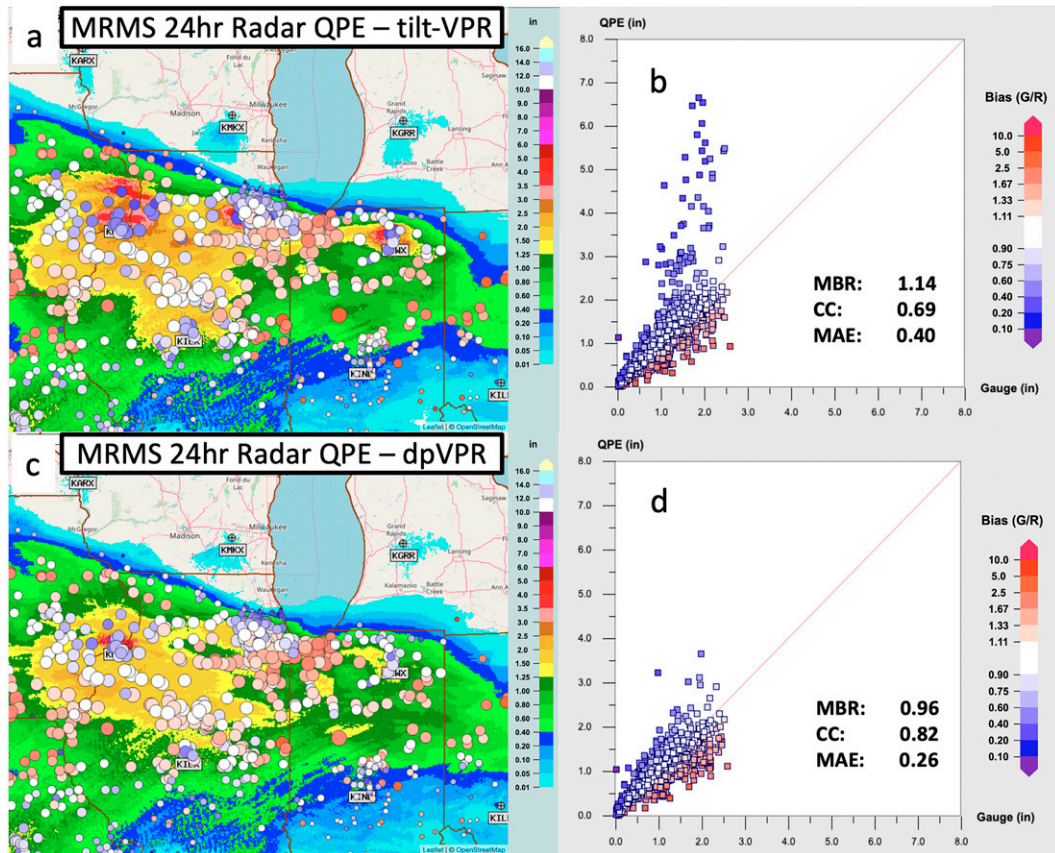
FIG. 19. 24-h radar QPEs ending at 1200 UTC 9 May 2021 with the (a) ZQ10 tilt-VPR and (c) dpVPR corrections and (b),(d) the corresponding gauge vs QPE scatterplots.

complete reflectivity correction due to the low and nonisotropic nature of the BB (black circle, Fig. 17b). This was not observed to the same degree in the dpVPR corrected QPE (Fig. 17c), which successfully delineated the BB and provided a relatively uniform reflectivity correction throughout the event. Consistent with other events, the dpVPR corrections provided an increase in QPE at far ranges compared to the tilt-VPR QPE, helping reduce the typical dry bias where radar beam is in the ice region of stratiform precipitation. However, both methodologies resulted in an overestimation of QPE to the southeast of the radar where the BB was well corrected (Figs. 17b,c versus Fig. 17a). The dpVPR corrected QPE had a wet bias (1.29) and a worse MAE (0.33 in., Fig. 17f) than the tilt-VPR QPE (0.27 in., Fig. 17e). A further investigation indicated that the default Z–R relationship of $Z = 75R^2$ was likely unrepresentative for the precipitation regime in this event. A study using local gauge and S-band profiler radar (Martner et al. 2008) in the northern California coastal area during December 2003 to February 2004 found a $Z = 210R^{1.46}$ relationship for the cool-season stratiform rain with BB in this region. Utilizing this R–Z relationship, the 24-h tilt-VPR and dpVPR QPEs near the radar are in closer agreement with the gauge amounts after reflectivity corrections (Figs. 18a,b versus Figs. 17b,c). The bias and MAE in the dpVPR corrected QPE improved

from 1.29 and 0.33 in. (Fig. 17f) to 0.97 and 0.24 in. (Fig. 18d), respectively. The MBR of the tilt-VPR corrected QPE worsened from 1.00 (Fig. 17e) to 0.73 (Fig. 18b) due to the severe underestimation at far ranges while the MAE remained unchanged at 0.27 in. (Fig. 18b). This event highlights the importance of appropriate R–Z relationships in addition to the VPR corrections for obtaining accurate QPEs.

e. Real-time results

The dpVPR scheme was implemented and evaluated in the real-time experimental MRMS system at the National Severe Storms Laboratory since March 2021. Figure 19 shows results from the operational (tilt-VPR) and the experimental (dpVPR) MRMS radar QPEs during a low BB event. The operational MRMS radar-based QPE (or Q3RAD), which utilizes the tilt-VPR methodology for reflectivity corrections, has severe overestimations near the KLOT and KDVN radars. As discussed before, when the BB is not fully visible due to being at the radar, the tilt-VPR methodology cannot fit an adequate VPR and does not provide sufficient reflectivity corrections. The experimental Q3RAD with a dpVPR correction alleviated much of this QPE overestimation near the radars. By including dual-pol variables, it is possible to determine that the
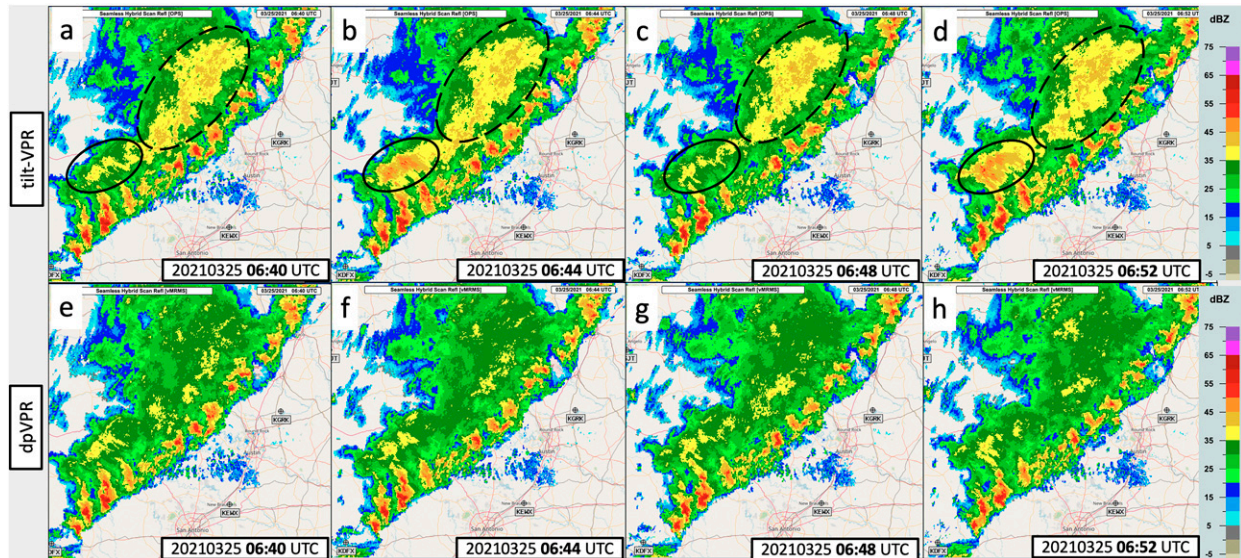
FIG. 20. MRMS seamless hybrid scan reflectivities corrected using the (a)–(d) ZQ10 tilt-VPR and (e)–(h) dpVPR. The dpVPR showed improved stability and consistency over the tilt-VPR in the reflectivity corrections from time to time.

BB is at the radar and likely not fully observed, and a conceptualized VPR can be fit to provide reflectivity corrections. At KDVN, the BB was particularly intense, and combined with errors in the model sounding data (sounding 0°C height was approximately 2 km, an overestimation), regions directly around the radar were misidentified as convection in the tilt-VPR and did not receive a reflectivity correction. As a result, some regions had an overestimation in QPE. For this event, the MBR decreased to 0.96 in the dpVPR QPE from 1.14 in the tilt-VPR QPE, and the MAE decreased to 0.26 in. from 0.40 in. (Figs. 19b,d).

Another advantage of the dpVPR methodology is the stability in reflectivity corrections through time. Dual-pol variables allow for more accurate and stable detections of the BB over reflectivity profiles alone. Figure 20 illustrates this for the stratiform region of an MCS. Although the tilt-VPR methodology was able to fit a VPR and apply corrections, the magnitude of corrections can change 5+ dBZ from one volume scan to the next (solid black circles, Figs. 20a–d). In other areas (dashed black circles, Figs. 20a–d), the full extent of the BB behind the leading convection was not consistently corrected by the tilt-VPR methodology. The dpVPR methodology (Figs. 20e–h) was able to correct the BB consistently in both regions, applying a stronger correction over a larger area than the tilt-VPR methodology. This resulted in a reduced overestimation bias (28% versus 6%) and MAE (0.073 versus 0.063 in.) from the tilt-VPR QPE to the dpVPR QPE (Fig. 21c versus Fig. 21d).

4. Summary and conclusions

A new dual-pol BB delineation and VPR correction methodology (dpVPR) was introduced to correct reflectivity observations within and above the melting layer for improved radar QPE. The BB delineation identifies the BB area using reflectivity and correlation coefficient fields for each tilt and define regions of reflectivity in need of a correction. The dpVPR methodology derives azimuthally dependent VPRs and then applies reflectivity corrections in real time. The use of ρ_{HV} and the delineated BBA allows for more localized reflectivity corrections with increased confidence in the melting layer bottoms and increases accuracy of reflectivity corrections in instances of nonisotropic and partly observed BB.

The proposed methodology was evaluated on 14 cases with varying BB heights, intensity, and symmetry. Additionally, the methodology was tested in real time on the MRMS testbed system. Case study and real-time events showed that the new dpVPR methodology provided increased accuracy compared to its predecessor (tilt-VPR) in the following ways: 1) 24-h QPE showed a reduction both in mean bias and in mean absolute error when validated against 24-h CoCoRaHS gauges; 2) the improvements were most significant in highly nonisotropic BB, and very low, partly observed BB, and were similar for warm-season events where the tilt-VPR methodology works well due to relatively high melting layers; 3) the dpVPR reduced dry biases at far ranges in stratiform rain where the lowest radar tilt was overshooting the melting layer; 4) reflectivity corrections were more stable between volume scans of radar data due to more accurate BB identification and VPR construction. Both VPR corrections were also compared to an empirical correction in the WSR-88D dual-pol digital precipitation rate QPE, which applies predefined multipliers to the rate field in areas within and above the bright band based on the hydrometeor classifications. It was found that the DPR QPE had significant challenges handling low and intense bright bands and resulted in larger overestimation errors than both of the tilt-VPR and dpVPR QPEs.
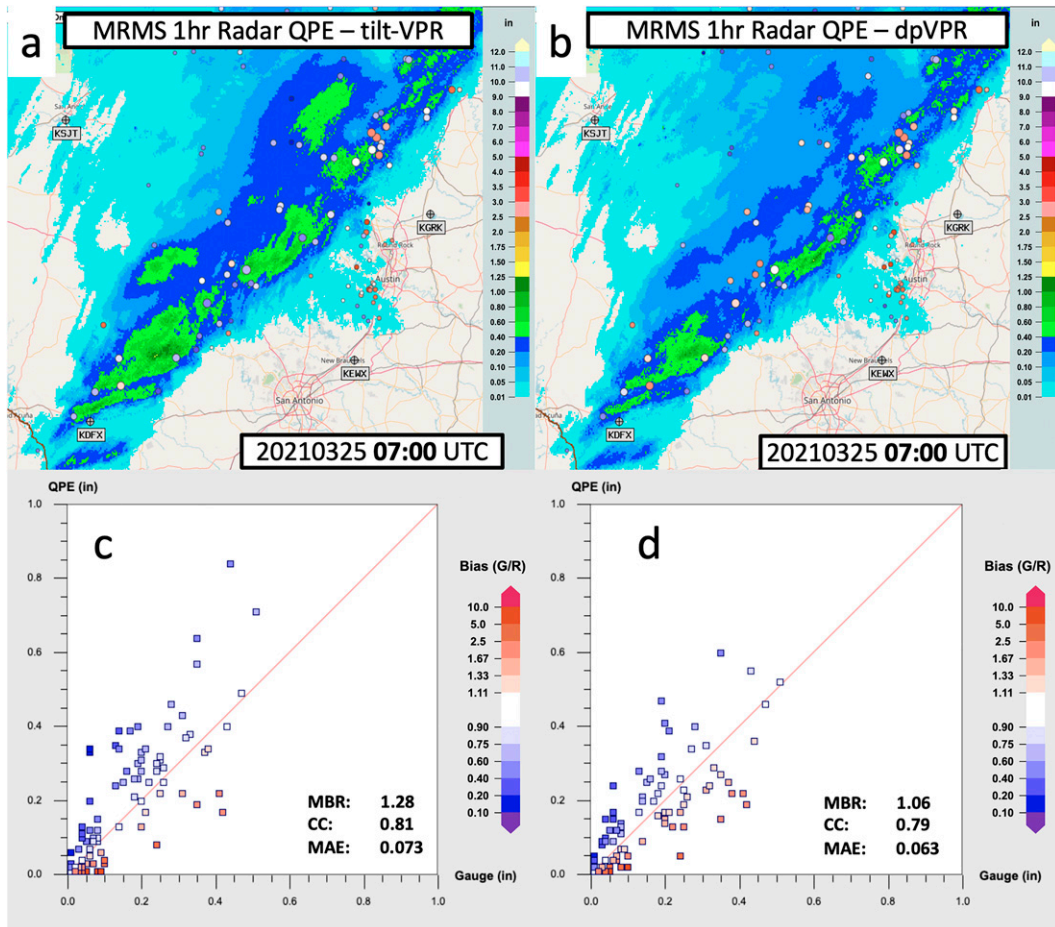
FIG. 21. Hourly MRMS mosaicked radar QPEs ending at 0700 UTC 25 Mar 2021 with the (a) ZQ10 tilt-VPR and (b) dpVPR corrections and (c),(d) the corresponding gauge vs QPE scatterplots.

The current dpVPR correction is only applied for stratiform rain areas where a BB peak could be identified and a reference BB bottom height and reflectivity are defined. When the surface precipitation is snow, the dpVPR correction was not applied although the radar beam overshooting effect still exists and can cause underestimation biases at far ranges (Koistinen 1991; Koistinen and Pohjola 2014). Future work will focus on the dpVPR correction of range-dependent radar QPE biases in snow.

REFERENCES

Andrieu, H., and J. D. Creutin, 1995: Identification of vertical profiles of reflectivity for hydrological application using an inverse method. Part I: Formulation. *J. Appl. Meteor.*, **34**, 225–239, https://doi.org/10.1175/1520-0450(1995)034<0225:IOVPOR>2.0.CO;2.

Benjamin, S. G., and Coauthors, 2016: A North American hourly assimilation and model forecast cycle: The rapid refresh. *Mon. Wea. Rev.*, **144**, 1669–1694, https://doi.org/10.1175/MWR-D-15-0242.1.

Chen, H., R. Cifelli, and A. White, 2020: Improving operational radar rainfall estimates using profiler observations over complex terrain in Northern California. *IEEE Trans. Geosci. Remote Sens.*, **58**, 1821–1832, https://doi.org/10.1109/TGRS.2019.2949214.

Cifelli, R., N. Doesken, P. Kennedy, L. D. Carey, S. A. Rutledge, C. Gimmestad, and T. Depue, 2005: The Community Collaborative Rain, Hail, and Snow Network: Informal education for scientists and citizens. *Bull. Amer. Meteor. Soc.*, **86**, 1069–1078, https://doi.org/10.1175/BAMS-86-8-1069.

Cocks, S. B., S. M. Martinaitis, B. Kaney, J. Zhang, and K. Howard, 2016: MRMS QPE performance during 2013/14 cool season. *J. Hydrometeor.*, **17**, 791–810, https://doi.org/10.1175/JHM-D-15-0095.1.

Fabry, F., and I. Zawadzki, 1995: Long-term radar observations of the melting layer of precipitation and their interpretation. *J. Atmos. Sci.*, **52**, 838–851, https://doi.org/10.1175/1520-0469(1995)052<0838:LTROOT>2.0.CO;2.

Fulton, R. A., J. P. Breidenbach, D.-J. Seo, D. A. Miller, and T. O'Bannon, 1998: The WSR-88D rainfall algorithm. *Wea. Forecasting*, **13**, 377–395, https://doi.org/10.1175/1520-0434(1998)013<0377:TWRA>2.0.CO;2.

Germann, U., G. Galli, M. Boscacci, and M. Bolliger, 2006: Radar precipitation measurement in a mountainous region. *Quart. J. Roy. Meteor. Soc.*, **132**, 1669–1692, https://doi.org/10.1256/qj.05.190.

Giangrande, S. E., and A. V. Ryzhkov, 2008: Estimation of rainfall based on the results of polarimetric echo classification. *J. Appl. Meteor. Climatol.*, **47**, 2445–2462, https://doi.org/10.1175/2008JAMC1753.1.

——, J. M. Krause, and A. V. Ryzhkov, 2008: Automatic designation of the melting layer with a polarimetric prototype of the WSR-88D radar. *J. Appl. Meteor. Climatol.*, **47**, 1354–1364, https://doi.org/10.1175/2007JAMC1634.1.

Helms, D., P. A. Miller, M. F. Barth, A. C. Darling, F. Kelly, and S. Koch, 2009: Status update of the transition from research to operations of the Meteorological Assimilation Data Ingest System. *25th Conf. on Int. Interactive Information and Processing Systems*, Phoenix, AZ, Amer. Meteor. Soc., 5A.3, https://ams.confex.com/ams/89annual/techprogram/paper_149883.htm.

Joss, J., and R. Lee, 1995: The application of radar–gauge comparisons to operational precipitation profile corrections. *J. Appl. Meteor.*, **34**, 2612–2630, https://doi.org/10.1175/1520-0450(1995)034<2612:TAORCT>2.0.CO;2.

——, A. Waldvogel, and C. G. Collier, 1990: Precipitation measurement and hydrology. *Radar in Meteorology*, D. Atlas, Ed., Amer. Meteor. Soc., 577–606.

Kitchen, M., 1997: Towards improved radar estimates of surface precipitation at long range. *Quart. J. Roy. Meteor. Soc.*, **123**, 145–163, https://doi.org/10.1002/qj.49712353706.

——, R. Brown, and A. G. Davies, 1994: Real-time correction of weather radar data for the effects of bright band, range, and orographic growth in widespread precipitation. *Quart. J. Roy. Meteor. Soc.*, **120**, 1231–1254, https://doi.org/10.1002/qj.49712051906.

Koistinen, J., 1991: Operational correction of radar rainfall errors due to vertical profile of reflectivity. Preprints, *25th Int. Conf. on Radar Meteorology*, Paris, France, Amer. Meteor. Soc., 91–96.

——, and H. Pohjola, 2014: Estimation of ground-level reflectivity factor in operational weather radar networks using VPR-based correction ensembles. *J. Appl. Meteor. Climatol.*, **53**, 2394–2411, https://doi.org/10.1175/JAMC-D-13-0343.1.

Krause, J. M., 2016: A simple algorithm to discriminate between meteorological and nonmeteorological radar echoes. *J. Atmos. Oceanic Technol.*, **33**, 1875–1885, https://doi.org/10.1175/JTECH-D-15-0239.1.

Marshall, J. S., R. C. Langille, and W. Mc. K. Palmer, 1947: Measurement of rainfall by radar. *J. Meteor.*, **4**, 186–192, https://doi.org/10.1175/1520-0469(1947)004<0186:MORBR>2.0.CO;2.

Martner, B. E., S. E. Yuter, A. B. White, S. Y. Matrosov, D. E. Kingsmill, and F. M. Ralph, 2008: Raindrop size distributions and rain characteristics in California coastal rainfall for periods with and without a radar bright band. *J. Hydrometeor.*, **9**, 408–425, https://doi.org/10.1175/2007JHM924.1.

Miller, P. A., M. Barth, L. Benjamin, R. Artz, and W. Pendergrass, 2007: MADIS support for UrbaNet. *14th Symp. on Meteorological Observation and Instrumentation/16th Conf. on Applied Climatology*, San Antonio, TX, Amer. Meteor. Soc., JP2.5, https://ams.confex.com/ams/87ANNUAL/webprogram/Paper119116.html.

Park, H.-S., A. V. Ryzhkov, D. S. Zrnić, and K.-E. Kim, 2009: The hydrometeor classification algorithm for the polarimetric WSR-88D: Description and application to an MCS. *Wea. Forecasting*, **24**, 730–748, https://doi.org/10.1175/2008WAF2222205.1.

Qi, Y., J. Zhang, D. Kingsmill, J. Min, and K. Howard, 2012: VPR corrections of cool season radar QPE errors in the mountainous area of Northern California. *IAHS Publ.*, **351**, 188–193.

——, ——, and P. Zhang, 2013: A real-time automated convective and stratiform precipitation segregation algorithm in native radar coordinates. *Quart. J. Roy. Meteor. Soc.*, **139**, 2233–2240, https://doi.org/10.1002/qj.2095.

——, ——, B. Kaney, C. Langston, and K. Howard, 2014: Improving WSR-88D radar QPE for orographic precipitation using profiler observations. *J. Hydrometeor.*, **15**, 1135–1151, https://doi.org/10.1175/JHM-D-13-0131.1.

Ryzhkov, A. V., M. Diederich, P. Zhang, and C. Simmer, 2014: Potential utilization of specific attenuation for rainfall estimation, mitigation of partial beam blockage, and radar networking. *J. Atmos. Oceanic Technol.*, **31**, 599–619, https://doi.org/10.1175/JTECH-D-13-00038.1.

Smyth, T. J., and A. J. Illingworth, 1998: Radar estimates of rainfall rates at the ground in bright band and non-bright band events. *Quart. J. Roy. Meteor. Soc.*, **124**, 2417–2434, https://doi.org/10.1002/qj.49712455112.

Steiner, M., R. A. Houze Jr., and S. E. Yuter, 1995: Climatological characterization of three-dimensional storm structure from operational radar and rain gauge data. *J. Appl. Meteor.*, **34**, 1978–2007, https://doi.org/10.1175/1520-0450(1995)034<1978:CCOTDS>2.0.CO;2.

Tabary, P., 2007: The new French operational radar rainfall product. Part I: Methodology. *Wea. Forecasting*, **22**, 393–408, https://doi.org/10.1175/WAF1004.1.

Tang, L., J. Zhang, C. Langston, J. Krause, K. Howard, and V. Lakshmanan, 2014: A physically based precipitation–nonprecipitation radar echo classifier using polarimetric and environmental data in a real-time national system. *Wea. Forecasting*, **29**, 1106–1119, https://doi.org/10.1175/WAF-D-13-00072.1.

——, ——, M. Simpson, A. Arthur, H. Grams, Y. Wang, and C. Langston, 2020: Updates on the radar data quality control in the MRMS quantitative precipitation estimation system. *J. Atmos. Oceanic Technol.*, **37**, 1521–1537, https://doi.org/10.1175/JTECH-D-19-0165.1.

Vignal, B., H. Andrieu, and J. D. Creutin, 1999: Identification of vertical profiles of reflectivity from volume scan radar data. *J. Appl. Meteor.*, **38**, 1214–1228, https://doi.org/10.1175/1520-0450(1999)038<1214:IOVPOR>2.0.CO;2.

——, G. Galli, J. Joss, and U. Germann, 2000: Three methods to determine profiles of reflectivity from volumetric radar data to correct precipitation estimates. *J. Appl. Meteor.*, **39**, 1715–1726.

Wang, Y., P. Zhang, A. V. Ryzhkov, J. Zhang, and P.-L. Chang, 2014: Utilization of specific attenuation for tropical rainfall estimation in complex terrain. *J. Hydrometeor.*, **15**, 2250–2266, https://doi.org/10.1175/JHM-D-14-0003.1.

Wilson, J. W., and E. A. Brandes, 1979: Radar measurement of rainfall: A summary. *Bull. Amer. Meteor. Soc.*, **60**, 1048–1058, https://doi.org/10.1175/1520-0477(1979)060<1048:RMORS>2.0.CO;2.

Zhang, J., and Y. Qi, 2010: A real-time algorithm for the correction of brightband effects in radar-derived QPE. *J. Hydrometeor.*, **11**, 1157–1171, https://doi.org/10.1175/2010JHM1201.1.

——, C. Langston, and K. Howard, 2008: Brightband identification based on vertical profiles of reflectivity from the WSR-88D. *J. Atmos. Oceanic Technol.*, **25**, 1859–1872, https://doi.org/10.1175/2008JTECHA1039.1.

——, and Coauthors, 2016: Multi-Radar Multi-Sensor (MRMS) quantitative precipitation estimation: Initial operating capabilities. *Bull. Amer. Meteor. Soc.*, **97**, 621–638, https://doi.org/10.1175/BAMS-D-14-00174.1.

——, L. Tang, S. Cocks, P. Zhang, A. Ryzhkov, K. Howard, C. Langston, and B. Kaney, 2020: A dual-polarization radar synthetic QPE for operations. *J. Hydrometeor.*, **21**, 2507–2521, https://doi.org/10.1175/JHM-D-19-0194.1.